Research Paper

Novel fluorinated Bi_2MoO_6 nanocrystals for efficient photocatalytic removal of water organic pollutants under different light source illumination

Changlin Yu [a],[*], Zhen Wu [a], Renyue Liu [a], Dionysios D. Dionysiou [b], Kai Yang [a], Chunying Wang [c], Hong Liu [d],[**]

[a] School of Metallurgy and Chemical Engineering, Jiangxi University of Science and Technology, Ganzhou 341000, China
[b] Environmental Engineering and Science Program, Department of Biomedical, Chemical and Environmental Engineering, University of Cincinnati, Cincinnati, OH 45221, United States
[c] School of Resources and Environmental Engineering, Jiangxi University of Science and Technology, Ganzhou 341000, China
[d] School of Chemical Engineering and Technology, Sun Yat-Sen University, Zhuhai, 519082, P.R. China

A R T I C L E   I N F O

A B S T R A C T

Development of efficient technologies to deal with organic pollutants in wastewater is an important issue. Photocatalysis, as a "green chemistry" technology, has attracted much attention in pollutants degradation and efficient visible-light-driven photocatalysts with powerful ability to completely oxidize organic pollutants in contaminated source water are highly desirable. Here, a series of fluorinated Bi_2MoO_6 crystals with different atomic ratio of F to Bi (R_F = 0.10, 0.15, 0.20, 0.25, 0.30) were prepared via a solvothermal-calcination process. The effects of F doping on the physicochemical properties of Bi_2MoO_6 were investigated by physicochemical techniques like XRD, N_2 adsorption, SEM, TEM, UV–Vis DRS, FT-IR, XPS, PL and photoelectrochemical measurement. The substitution of F^- anions for the host O^{2-} anions induced the lattice shrinkage, a decrease in crystal size and an increase in crystallinity. Moreover, the oxygen vacancies in F-Bi_2MoO_6 and F^- adsorbed over the catalyst surface could withdraw the photoexcited electrons, largely boosting the separation of photoexcited electron–hole pairs. $F_{0.20}$-Bi_2MoO_6 displayed significant photocatalytic performance in removal of phenol, bisphenol A, 4-chlorophenol and Rhodamine B dye. ESR and radicals trapping confirmed holes are mainly responsible for the degradation of the target organic pollutants. However, $\cdot OH$ and $\cdot O_2^{2-}$ could be also involve in photocatalytic reactions. Meanwhile, the more positive potential of VB in F-Bi_2MoO_6 could promote the oxidation power of the h^+ in organic pollutants removal.

1. Introduction

Over the past decades, the organic pollutants in water discharged by textile industries and other chemical industries have become a major source of environmental pollution in water. Organic pollutants such as phenol, bisphenol A and 4-chlorophenol may cause various adverse effects on aquatic organisms even at low exposure levels. For example, bisphenol A [2,2-bis(4-hydroxyphenyl)propane, BPA] is one of the typical endocrine disrupting chemicals [1] and 4-chlorophenol can easily contaminate the soil and water due to its toxicity, ability to bioaccumulate in the food chain, and persistence in the environment [2]. However, it is difficult to eliminate these organic pollutants with conventional water treatment process. Such pollutants can only be decomposed very slowly by acids, highly alkaline solutions, heating, or biological methods. Photocatalytic degradation, as an advanced oxidation technology, is a promising method in organic pollutants degradation due to its extremely efficient degradation rate, high mineralization efficiency, and low toxicity of some of the catalysts used such as TiO_2. Photocatalysis ideally leads to CO_2, H_2O, and other minerals as the end-products [3–9]. Upon irradiation of light with photon energy greater than or equal to the band gap energy of the photocatalyst, the electron (e^-)–hole (h^+) pairs are initiated. The photogenerated e^- and h^+ migrate to the surface and react with the adsorbed species over the surface of photocatalyst to produce the active radicals ($\cdot O_2^-$, $\cdot OH$, h^+, etc.). These radicals possess

strong ability to destroy or mineralize different organic contaminants, e.g. 6-hydroxymethyl uracil [10], dinitrophenol [11], phenol [12], bisphenol A [13], trichlorophenol [14], spiramycin [15], aromatic organoarsenic compounds [16], levofloxacin drug [17], flame retardant [18], cyanotoxins [19–21], and etc.

The decomposition or mineralization efficiency of organic pollutants is mainly determined by the semiconductor photocatalysts and the molecular properties of pollutants. Moreover, the photocatalytic performance of photocatalysts strongly depends on their optical absorption properties and microstructures, e.g. crystallinity, surface area, crystal phase, crystal plane, and morphologies. Up to now, TiO_2 semiconductor is the most investigated and applied photocatalyst due to its chemical stability, low cost, and nontoxicity. However, because of its large band gap energy ($\sim$3.2 eV), thus only ultraviolet light fraction in solar light can be absorbed by TiO_2. So, TiO_2 is not an ideal photocatalyst to efficiently utilize sunlight in naturally environmental purification or remediation [22,23].

Nowadays, many efforts have been devoting to developing high efficient visible light harvesting photocatalysts. Some novel and efficient visible light response semiconductors, e.g. g-C_3N_4 [24], Ag_2O/Ag_2CO_3 [25], $Au_{25}(SR)_{18}$/TiO_2 [26], and $CsPbBr_3$ [27,28], have been explored in recent years. Among the visible-light-driven photocatalysts, Bi-based photocatalysts such as Bi_2O_3 [29], BiOX(X = Cl,Br,I) [30], $BiVO_4$ [31], $BiPO_4$ [32], Bi_2WO_6 [33], and Bi_2MoO_6 [34] have attracted much attention due to their attractive visible light absorption and eco-friendly characteristics. Bi_2MoO_6 is an important Bi-based semiconductor, belonging to the typical members of the Aurivillius oxide family. It possesses an appropriate band gap energy ($\sim$2.7 eV) which enables it to capture visible light and display promising photocatalytic performance for water splitting and degradation of organic pollutants [35,36]. However, relatively low quantum yield and rapid recombination of photoinduced charge carriers still limit its practical application [37,38]. To resolve these issues, different strategies were put forward, e.g. design heterojunction, morphology control, semiconductor coupling, noble metal nanoparticles (NPs) deposition, and element doping. For example, a flower-like Bi_2S_3/Bi_2MoO_6 heterojunction with low probability of e^-–h^+ recombination and high photocatalytic activity were reported by Zhang et al. [35]. At the same time, Feng et al. [39] successfully synthesized a novel CdS/Bi_2MoO_6 heterojunction photocatalyst via two-step hydrothermal methods. The obtained CdS/Bi_2MoO_6 displayed enhanced separation efficiency of photogenerated e^- and h^+ with respect to bare Bi_2MoO_6 and CdS. Besides the construction of heterojunction to enhance the photocatalytic performance, element doping is another effective strategy for improving the photocatalytic properties. Ding et al. [40] reported a Bi doped Bi_2MoO_6 and they found that Bi self-doping could not only promote the separation and transfer of photogenerated e^-–h^+ pairs, but also alter the position of valence and conduction band. Our recent research indicated that rare earth Gd^{3+} doping induced a contraction of lattice and a decrease in crystallite size of Bi_2MoO_6 [41]. Meanwhile, an increase in surface area and an enhancement in visible light harvesting occurred. Another rare earth Ce doped Bi_2MoO_6 was reported by Dai et al. [42]. They discovered that the variation of Ce dopant content in the host Bi_2MoO_6 lattice could result in distinctly improved visible-light-driven photocatalytic performance for the degradation of highly toxic nerve agent simulants (NAS) and organic dyes, as well as bacterial photoinactivation. Other element doping such as with Zn^{2+} [43] and B [44] was also reported.

Here, aiming at the design of efficient solar energy driven Bi_2MoO_6 photocatalysts for organic contaminant removal, the effects of fluorination on the texture, crystal, band structures, and optical properties of Bi_2MoO_6 crystals were investigated in detail. In addition, the photocatalytic performance of F-Bi_2MoO_6 in the removal of various organic pollutants in water, specifically Rhodamine B dye, phenol, bisphenol A, and 4-chlorophenol, was explored under different radiation wavelength light sources. F-Bi_2MoO_6 displayed a large enhancement in degradation efficiency compared with pure Bi_2MoO_6. Our results might allow us to provide an instructive guidance for developing non-toxic and efficient visible-light-driven Bi_2MoO_6-based photocatalysts for removal of organic pollutants in water.

2. Experimental

2.1. Catalyst preparation

Materials and reagents. $Bi(NO_3)_3 \cdot 5H_2O$, $(NH_4)_6Mo_7O_{24} \cdot 4H_2O$, NaF, ethylene glycol, Rhodamine B, phenol, P-chlorophenol were of analytical grade and purchased from Sinopharm Chemical Reagent Co. Ltd. China. BPA (purity 99.5%), was purchased from Dr. Ehrenstorfer GmbH, Augsburg, Germany. The reagents used for mobile phase of high performance liquid chromatography (HPLC) included HPLC-grade methanol and acetonitrile, both from Dikma Chemical (China), and Mill-Q ultrapure water.

Preparation of Bi_2MoO_6 and F-Bi_2MoO_6. Samples were prepared via a solvothermal-calcination process. Under sonication, a specific amount (1.94 g) of $Bi(NO_3)_3 \cdot 5H_2O$ was first dissolved in 70 mL ethylene glycol. Then under magnetically stirring, 0.35 g of $(NH_4)_6Mo_7O_{24} \cdot 4H_2O$ and stoichiometric NaF (with the molar ratio of F to Mo (F_R) at 0.10, 0.15, 0.20, 0.25, 0.30, respectively) were added and the pH value of ethylene glycol solution was adjusted to 7.0. After stirring for 30 min, the solution was placed in a Teflon-lined stainless autoclave and heated to 160 °C and maintained for 10 h. The obtained powder was collected, washed three times with distilled water and dried at 110 °C for 12 h. Finally, the powder was placed in a furnace and calcined at 400 °C for 2 h and the obtained F-Bi_2MoO_6 was denoted as F_R-Bi_2MoO_6 (R: atomic ratio of F to Mo, R = 0.10, 0.15, 0.20, 0.25, 0.30, respectively).

2.2. Catalyst characterization

Powder X-ray diffraction data were recorded at a scanning rate of 0.05°/s using a Bruker D8-advance X-ray diffractometer at 40 kV and 40 mA for Cu $K\alpha$ radiation (λ = 0.15418 nm). The Brunauer–Emmett–Teller (BET) surface areas of the sample were obtained from N_2 adsorption/desorption isotherms determined at liquid nitrogen temperature (77 K) on an automatic analyzer (ASAP 2020). The samples were outgassed for 2 h under vacuum at 180 °C prior to adsorption. Scanning electron microscopy (SEM) of sample was measured with FLA650F type of the FEI company. Transmission electron microscopy (TEM) and high-resolution transmission electron microscopy (HRTEM) images were recorded on a Tecnai 20 FEG microscope. UV–Vis diffuse reflectance spectra (DRS) were measured using a UV–Vis spectrophotometer (UV-2550, Shimadzu). Fourier transform infrared (FT-IR) spectra were recorded with a Nicolet 5700 FT-IR spectrometer. Samples were pressed by a KBr disk preparation apparatus. The surface composition was determined by X-ray photoelectron spectroscopy (XPS) using a PHI Quantum 2000 XPS system with a monochromatic Al Ka source and a charge neutralizer. All the binding energies were referenced to the C1s peak at 284.8 eV of the surface adventitious carbon. The photoluminescence (PL) emission spectra of the samples were recorded on a fluorescence spectrometer (Hitachi F-4500, Japan). The electron spin resonance (ESR) spectra were recorded on an electron spin resonance spectrometer (Bruker ER200-SLC, Germany) with 5,5-dimethyl-1-pyrroline N-oxide (DMPO: 50 mM, 0.2 mL) in the aqueous with suspended photocatalyst. The settings for ESR spectrometer were as follows: center field = 323.467 mT, sweep width = 5 mT, microwave

frequency = 9069 MHz, and microwave power = 0.998 mW. Photocurrent and Mott–Schottky measurements were carried out on an electrochemical workstation with three-electrode (CHI-660E, China). 0.1M Na_2SO_4 solution was used as electrolyte solution. Saturated Ag/AgCl and platinum wires were utilized as reference electrodes and the counter electrode, respectively. The working electrode is the sample films coated on indium tin oxide (ITO) conducting glass. The homogeneous mixtures of 1 mL ethanol and 10 mg samples were coated over ITO and dried at 100 °C for 5 h. An 300 W xenon lamp was utilized as the excitation light source.

2.3. Studies on the degradation of organic pollutants

The photocatalytic degradation experiments were carried out in a photochemical reactor (Fig. S1). In Rhodamine B degradation, 50 mg photocatalyst was suspended in 100 mL RhB (20 mg/L) aqueous solution. A 500 W xenon lamp (Solar-500N) was used as the simulated solar light source. Before reaction, the suspension was magnetically stirred in the dark for 40 min to ensure adsorption equilibrium of RhB on the catalysts. The system was cooled by circulating water and maintained at room temperature. Approximately 2 mL suspension was sampled and centrifuged for RhB analysis by a UV–Vis spectrophotometer. The procedure for the degradation of the other target organic pollutants, e.g. phenol (20 mg/L), bisphenol A (20 mg/L), and 4-chlorophenol (20 mg/L), was the same as that described above. The pH values for the solutions of RhB, phenol, bisphenol A and 4-chlorophenol are 7.01, 7.02, 7.42, and 7.46, respectively. The concentrations of phenol, bisphenol A and 4-chlorophenol in the reaction solution were quantified by a high performance liquid chromatograph (HPLC, Sykam, German). Phenol, bisphenol A and P-chlorophenol in the reaction solution was analyzed on a HPLC instrument (Sykam, Germany) equipped with fluorescence fetector and a Waters XTerra RP18 column (3.9 mm × 150 mm, particle size 5 μm). The mobile-phase was 70% methanol and 30% water with a flow rate of 0.5 mL min^{-1}. Total organic carbon (TOC) was measured with a (Vario TOC, German Elementar Company) analyzer. The removal ratio (R) of phenol, bisphenol A and 4-chlorophenol (or TOC) was determined as follows:

$$R = (1 - C/C_0) \times 100\% \qquad (1)$$

Where C_0 is the initial concentration of phenol, bisphenol A and P-chlorophenol (or TOC) and C is the concentration at reaction time t (min).

Total organic carbon (TOC) was measured with a vario TOC analyzer (Vario TOC, German Elementar Company). Moreover, different light sources, e.g. simulated sunlight source (500 W xenon lamp, Solar-500N), visible light source with a cut-on (or long pass) filter at 400 nm was used as visible light source and ultraviolet light source with a cut-on filter (<400 nm)were applied.

3. Results and discussion

3.1. Texture properties

Fig. 1(a) shows that the diffraction peaks at 2θ of 28.3°, 32.6°, 47.2° and 55.6° are assigned to the crystal planes of (131), (200), (260) and (133) of orthorhombic Bi_2MoO_6(JCPDS No.76-2388), respectively. No characteristic peaks of other impurities can be found. With fluorine doping, the crystal phase did not change, but an increase in crystallinity obviously occurred. A similar phenomenon was reported on the fluorinated Bi_2O_3 [45] probably caused by the mediating role of fluoride ions in the dissolution and recrystallization processes of metastable crystal intermediates.

As observed in all samples, a careful comparison of the (131) diffraction peaks in the range of 2θ = 28.25–28.40° shown in
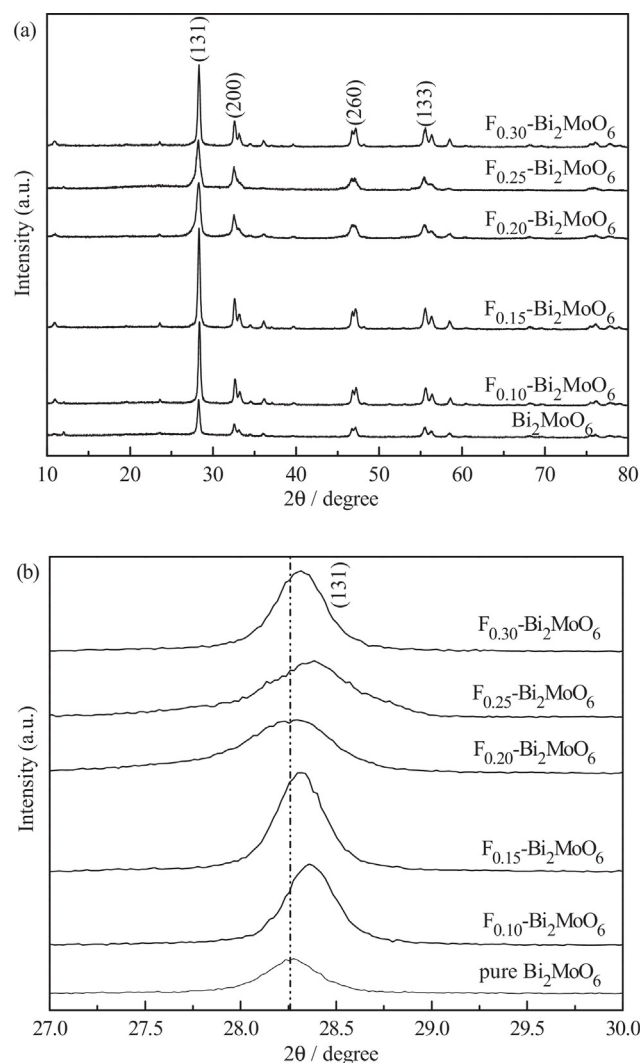

Fig. 1. XRD patterns of the prepared samples. (a) Survey patterns of Bi_2MoO_6 and F_R-Bi_2MoO_6; (b) Magnified patterns of (131) crystal plane of Bi_2MoO_6 and F_R-Bi_2MoO_6.

Fig. 1(b) (magnified (131) peak) suggests that the peak position of Bi_2MoO_6 with the increase of fluorine content shifted slightly toward a higher 2θ value. The same results were also observed in the other diffraction peaks. Based on Bragg's law, $d_{(hkl)} = n\lambda/(2sin\theta)$, where $d_{(hkl)}$ is the distance between crystal planes of $(h\,k\,l)$, λ is the X-ray wavelength, and θ is the diffraction angle of the crystal plane $(h\,k\,l)$, the observed shift of the diffraction peaks to a higher angle directly reflects the lattice shrinkage of the detected crystals [46]. The lattice shrinkage well suggests the substitution of the foreign F^- anion with smaller size (0.133 nm) for the host O^{2-} anion with larger size (0.140 nm) in the Bi_2MoO_6 host after the fluorination. Besides, F^- doping as the interstitial dopants could lead to an increase in lattice parameter due to the repulsion between F^- anions, which has been observed from the fluorinated $ZnWO_4$ [47] and Bi_2WO_6 [48].

Here, the strongest diffraction peak (131) was selected to estimate the average grain size of the bare Bi_2MoO_6 and F_R-Bi_2MoO_6 samples through the Scherrer equation: $D = 0.89\lambda/(\beta cos\theta)$. The results (Table 1) reveal that F doping brought about a slight decrease in average grain size, which is more distinct for $F_{0.20}$-Bi_2MoO_6 and $F_{0.25}$-Bi_2MoO_6 samples. So the fluorination on Bi_2MoO_6 in the present case not only introduces fluorine as substituting anion into the Bi_2MoO_6 host but also improves the crystallinity and decreases the grain size of Bi_2MoO_6 crystal. However, F doping gave rise

Table 1
Average crystallite sizes and specific surface areas of the prepared samples.

Sample	Average crystallite size (nm)	Specific surface area (m^2/g)
Bi_2MoO_6	22.6	16.9
$F_{0.10}$-Bi_2MoO_6	20.0	12.8
$F_{0.15}$-Bi_2MoO_6	19.6	11.7
$F_{0.20}$-Bi_2MoO_6	13.3	15.3
$F_{0.25}$-Bi_2MoO_6	16.4	14.6
$F_{0.30}$-Bi_2MoO_6	19.0	13.6

to an adverse effect on surface area and the surface area slightly decreased from 16.9 to 11.7 m^2/g. The reason for the decrease in specific surface area of Bi_2MoO_6 after doping may be ascribed to an increase in the crystallinity of Bi_2MoO_6.

3.2. Morphologic structure

SEM and TEM analyses were applied to analyze the morphology and crystal for bare and F doped samples. As shown in Fig. 2(a), pure Bi_2MoO_6 is composed of small particles with no regular morphology. The F doping made the small and irregular Bi_2MoO_6 particles become large particles with more regular sheet-like morphology, as shown in Fig. 2(b) and (c).

These sheet-like particles possess smooth surface, which could lead to the small surface area. Low resolution TEM image in Fig. 3(a) shows that the size of prime Bi_2MoO_6 particles is not uniform, varying from 10 to 40 nm and some particles appear to exhibit sheet-like morphology. F doping only slightly alters the morphology of Bi_2MoO_6 prime particles with more regular nanosheet morphology, as shown in Fig. 3(b). The HRTEM images of Bi_2MoO_6 and $F_{0.20}$-Bi_2MoO_6 illustrate the high crystallinity of these two samples. In Fig. 3(c), the lattice spacing of 0.321 nm corresponds to the crystal plane of (041) in Bi_2MoO_6 (JCPDS No.72-2388). Whereas, in Fig. 3(d), the lattice spacing of (041) crystal plane is 0.304 nm which is slightly smaller than that of Bi_2MoO_6, which could be due to the lattice shrinkage of Bi_2MoO_6 induced by the substitution of lattice O^{2-} by F^-. Another clear lattice spacing (0.308 nm) of (131) crystal plane was also observed. This lattice spacing is also smaller than that of the standard lattice spacing of (131) crystal plane of Bi_2MoO_6 (0.315 nm), which may be caused by the lattice contraction due to F doping.

The distribution of individual elements over the $F_{0.20}$-Bi_2MoO_6 sample particles had characterized using elemental mapping technique. Fig. 4(b) reveals the $F_{0.20}$-Bi_2MoO_6 sample particles include Bi, Mo, O and F elements and Fig. 4(c)–(f) shows the corresponding elemental mapping images, in which we can clearly see the uniform distribution of Bi, Mo, O and F elements in the $F_{0.20}$-Bi_2MoO_6 sample.

3.3. Optical absorption property

UV–Vis DRS of pure Bi_2MoO_6 and F_R-Bi_2MoO_6 composites are presented in Fig. 5. The absorption edge of bare Bi_2MoO_6 is around 510 nm, indicating that Bi_2MoO_6 possesses strong photoabsorption from the UV to visible-light region. Fluorine doping slightly affected the light absorption of Bi_2MoO_6 crystal and led to an obvious blue-shift in the absorption threshold, indicating an increase in the band gap. The band gap energies for the present series of catalysts were determined with Tauc's law from the intercept of a straight line fitted through the rise of the function $[F(Ra)h\nu]^2$ plotted versus $h\nu$, where $F(Ra)$ is a Kubelka–Munk function and $h\nu$ is the energy of the incident photon [49]. The obtained results are shown in Fig. 5. The approximate band gap energies of the resulting samples are ~2.71 eV for Bi_2MoO_6 and 2.73–2.78 eV for F_R-Bi_2MoO_6, respectively.

3.4. Composition and chemical state analysis

The survey XPS spectrum of $F_{0.20}$-Bi_2MoO_6 sample is presented in Fig. 6(a), showing the existence of F, Bi, O, and Mo elements. The atom percentage of Bi, Mo, O, and F was estimated around 21.70%, 10.82%, 65.28% and 1.89%, respectively, which is almost consistent with the composition of $F_{0.20}$-Bi_2MoO_6. Fig. 6(b) shows that there was an overlap of F 1s and Bi 4p XPS spectra. There are two types of fluorine species in the $F_{0.20}$-Bi_2MoO_6. One peak at the binding energy of 683.0 eV is attributed to fluoride anions adsorbed on the catalyst surface; another peak at the binding energy of 688.4 eV is assigned to the substitutional F^- atoms that occupied oxygen sites in the Bi_2MoO_6 crystal lattice [50,51]. Apparently, the F content on the host surface is much more than that in the host lattice. Under hydrothermal condition, tiny Bi_2MoO_6 crystalline nuclei in a supersaturated medium formed, and the crystal growth then followed. One fraction of F^- ions by the substitution of O^{2-} could be directly introduced to the resulting sample as the doping of the crystal lattice. Instead, the other fraction of F^- ions in the solution could interact strongly with the surface of the Bi_2MoO_6 crystal as fluoride anions adsorbed on the catalyst surface. The binding energies of Bi 4f at 159.1 eV for Bi $4f_{7/2}$ and 164.3 eV for Bi $4f_{5/2}$ are indexed to a trivalent oxidation state for bismuth [37]. The binding energies of 232.4 eV and 235.5 eV are corresponding to Mo $3d_{3/2}$ and Mo $3d_{5/2}$, respectively. The O 1s region can be fitted into two peaks at 530.0 eV and 530.8 eV, respectively. These two peaks are indexed to the lattice O^{2-} in the Bi_2MoO_6 and hydroxyl groups on the surface of the sample, respectively.

3.5. PL properties

PL emission spectra of semiconductor photocatalyst can effectively reflect the efficiency of charge carrier trapping, migration,
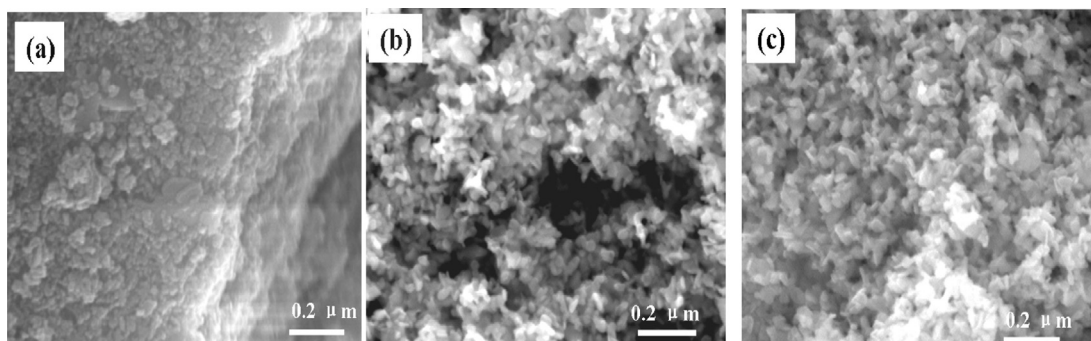

Fig. 2. SEM images of the typical samples. (a) Bi_2MoO_6; (b) $F_{0.10}$-Bi_2MoO_6; (c) $F_{0.20}$-Bi_2MoO_6.

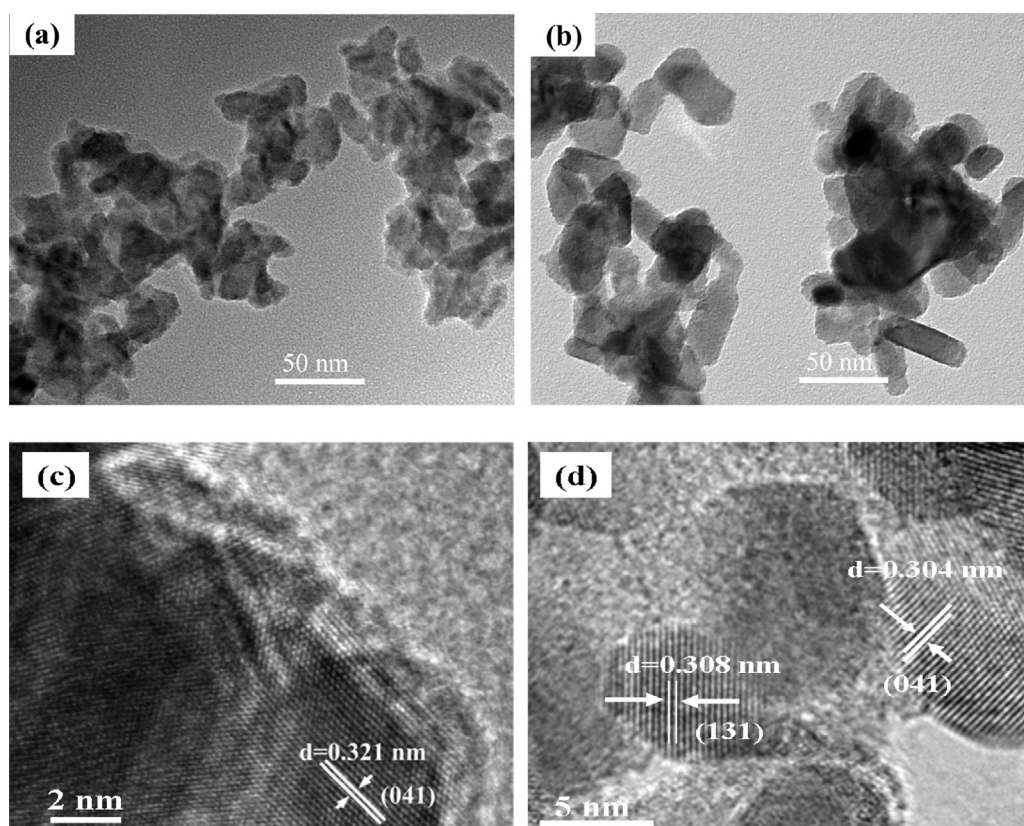**Fig. 3.** Low and high resolution TEM images of the Bi_2MoO_6 and $F_{0.20}$-Bi_2MoO_6 samples. (a) Low resolution TEM image of pure Bi_2MoO_6; (b) Low resolution TEM image of $F_{0.20}$-Bi_2MoO_6; (c) High resolution TEM image of Bi_2MoO_6; (d) High resolution TEM image of $F_{0.20}$-Bi_2MoO_6.
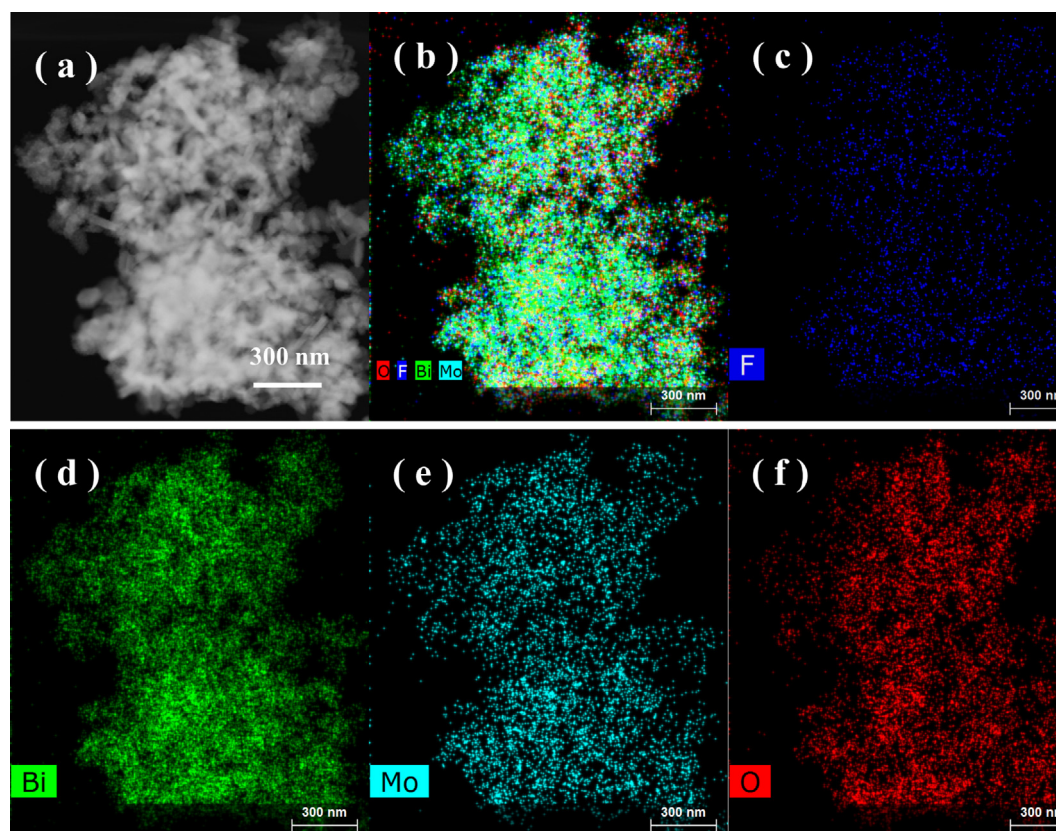
Fig. 4. STEM image and the elemental mapping images of $F_{0.20}$-Bi_2MoO_6. (a) STEM image of $F_{0.20}$-Bi_2MoO_6, the element mapping of (b) all, (c) F, (d) Bi, (e) Mo, (f) O elements.
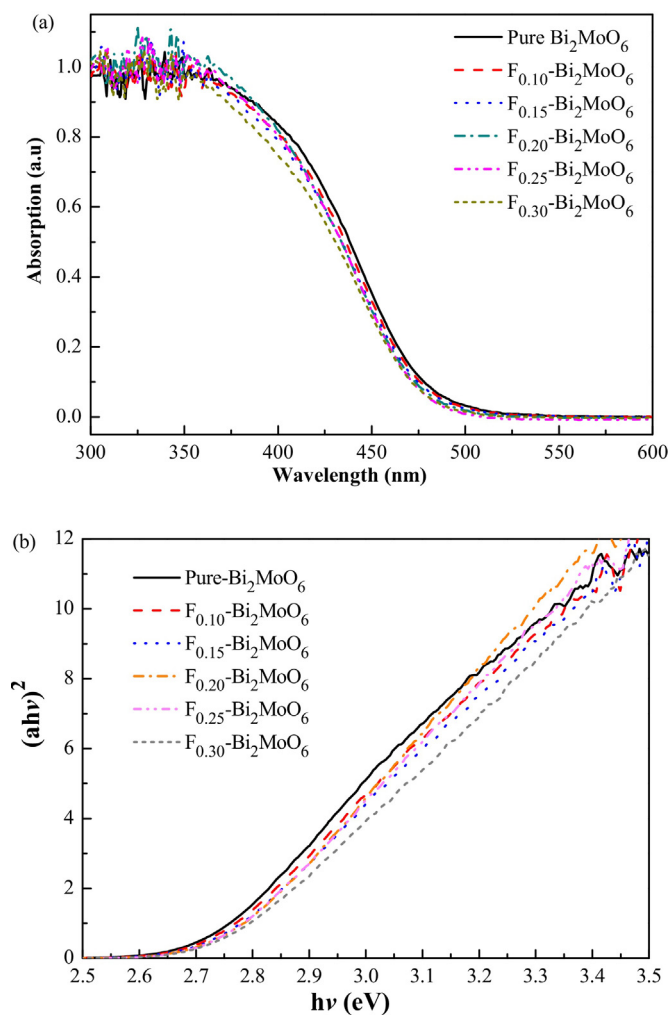
Fig. 5. (a) UV–Vis absorption spectra of the prepared pure Bi_2MoO_6 and F_R-Bi_2MoO_6 samples; (b) The curves of $(ahv)^2$ versus hv for pure Bi_2MoO_6 and F_R-Bi_2MoO_6.

and transfer, which indirectly reveals the fate of electron-hole pairs [52]. Fig. 7 presents the room temperature PL spectra of the as-prepared pure Bi_2MoO_6 and F_R-Bi_2MoO_6 samples with excitation wavelength of 350 nm. PL spectra clearly indicated an emission peak centered at around 525 nm. Moreover, the intensity of PL peak was effectively decreased by F^- doping and fluorinated Bi_2MoO_6 ($R_F = 0.2$) showed the weakest intensity. Lower PL intensity usually indicates the lower recombination rate of photo-generated electron-hole pairs. In this fluorinated Bi_2MoO_6, more oxygen vacancies could be produced because F^- ions have a much stronger affinity for electrons compared with O^{2-} ions. It can be speculated that the electronic cloud deviates from the original position in a Bi–O polyhedron containing fluorine, and the bonds between Bi and O could be weakened in F_R-Bi_2MoO_6 [48]. Therefore, plenty of oxygen vacancies are easily produced with the illumination of light in F_R-Bi_2MoO_6. Moreover, the F^- over the fluorinated surface of Bi_2MoO_6 would serve as an electron-trapping site and benefit the enhancement of interfacial electron-transfer rates by tightly holding trapped electrons.

3.6. Photoelectrochemical property

To further compare the interfacial charge transfer between pure Bi_2MoO_6 and F_R-Bi_2MoO_6 samples, photoelectrochemical experiments were carried out [53]. As seen from Fig. 8, the photocurrent intensity of F_R-Bi_2MoO_6 is higher than that of pure Bi_2MoO_6. The order of photocurrent intensity is as follows: $F_{0.20} > F_{0.25} > F_{0.30} > F_{0.15} > F_{0.10} > F_0$. The obviously enhanced photocurrent of F_R-Bi_2MoO_6 indicates that the separation efficiency of electron-hole pairs is improved over fluorinated Bi_2MoO_6, which is almost consistent with the PL analysis.

3.7. Degradation efficiency of the Bi_2MoO_6 and F_R-Bi_2MoO_6

The photocatalytic performances of the pure Bi_2MoO_6 and F_R-Bi_2MoO_6 samples were first evaluated in the degradation of RhB dye under xenon lamp irradiation (simulated sunlight, UV–Vis light). The variations in RhB concentration profiles (expressed as normalized concentration C/C_0) under light irradiation are show in Fig. 9. All of the as-prepared samples display the strong ability to degrade RhB. Obviously, F_R-Bi_2MoO_6 (x = 0.10, 0.15, 0.20, 0.25, 0.30, respectively) composites exhibit significantly higher activities than bare Bi_2MoO_6 indicating that the fluorination is an efficient method for enhancing the photocatalytic activity of Bi_2MoO_6. The degradation (expressed as %removal) of RhB over pure Bi_2MoO_6 is only ~34%. The corresponding values of RhB removal (%) are 38%, 59%, 78%, 73% and 63%, for $F_{0.10}$-Bi_2MoO_6, $F_{0.15}$-Bi_2MoO_6, $F_{0.20}$-Bi_2MoO_6, $F_{0.25}$-Bi_2MoO_6 and $F_{0.30}$-Bi_2MoO_6, respectively. With optimum molar ratio of $R_F = 0.2$(F/Mo), about 1.3 time increase in removal (%) of RhB with respect to pure Bi_2MoO_6 was obtained.

To further evaluate the photocatalytic degradation ability of Bi_2MoO_6 and F_R-Bi_2MoO_6, degradation and mineralization studies on other water organic pollutants (phenol, bisphenol A and 4-chlorophenol) were carried out over pure Bi_2MoO_6 and F_R-Bi_2MoO_6 under different light sources irradiation in Fig. 10. All the results of photocatalytic ability are as follows: $F_{0.20}$-$Bi_2MoO_6 > F_{0.25}$-$Bi_2MoO_6 > F_{0.30}$-$Bi_2MoO_6 > F_{0.15}$-$Bi_2MoO_6 > F_{0.10}$-$Bi_2MoO_6 > Bi_2MoO_6$. Among them, the photocatalytic degradation ability of $F_{0.20}$-Bi_2MoO_6 to phenol, bisphenol A and 4-chlorophenol exhibit the highest activity. Under Vis, UV, and UV–Vis light irradiation, the photocatalytic % removal of phenol were 45.3%, 53.0% and 80.7%, respectively, and the mineralization rate of phenol reached 44.5%, 52.9% and 80.2%, respectively (Fig. 10(a) and (e)). However, under simulated sunlight irradiation, the % removal and the %mineralization of phenol over pure Bi_2MoO_6 were only ~15.1% and ~7.4%, respectively, which suggests that F doping brings about the powerful degradation and mineralization ability of $F_{0.20}$-Bi_2MoO_6 to phenol under simulated sunlight irradiation conditions. Further studies in decomposition of bisphenol A show that both Bi_2MoO_6 and $F_{0.20}$-Bi_2MoO_6 can degrade bisphenol A. However, as shown in Fig. 10(b) and (e), $F_{0.20}$-Bi_2MoO_6 also could enhance the removal of bisphenol A compared with the pure Bi_2MoO_6. With respect to pure Bi_2MoO_6, under Vis, UV, and UV–Vis light irradiation, the %removal of bisphenol A over $F_{0.20}$-Bi_2MoO_6 increased from 36.3 to 74.7%, 48.6 to 87.9% and 54.1 to 98.3%, respectively, and the %mineralization of bisphenol A increased from 13.57 to 41.2%, 39.47 to 67.11% and 45.16 to 77.81%, respectively. Similarly, $F_{0.20}$-Bi_2MoO_6 displayed high efficiency in degradation of bisphenol A. Under simulated sunlight irradiation, % degradation and % mineralization of 4-chlorophenol (Fig. 10(c) and (f)) over $F_{0.20}$-Bi_2MoO_6 reached 33.6% and 28.6%, respectively, which shows that 4-chlorophenol is more resistant to photocatalytic degradation.

The pseudo-first order kinetic model as expressed by $\ln(C_0/C) = kt$, was used to describe the kinetics of organic pollutants degradation and the results are shown in Fig. S2 and Table S1. It indicates that the degradation rate constant of RhB over $F_{0.20}$-Bi_2MoO_6 (0.0149 min^{-1}) is 3.5 times higher with respect to pure Bi_2MoO_6 (0.0043 min^{-1}) under simulated sunlight irradiation. The degradation rate constants of phenol over $F_{0.20}$-Bi_2MoO_6 increased 8.9, 8.8, and 9.1 times with respect to pure Bi_2MoO_6 under visible light, ultraviolet light, and simulated sunlight irradiation,
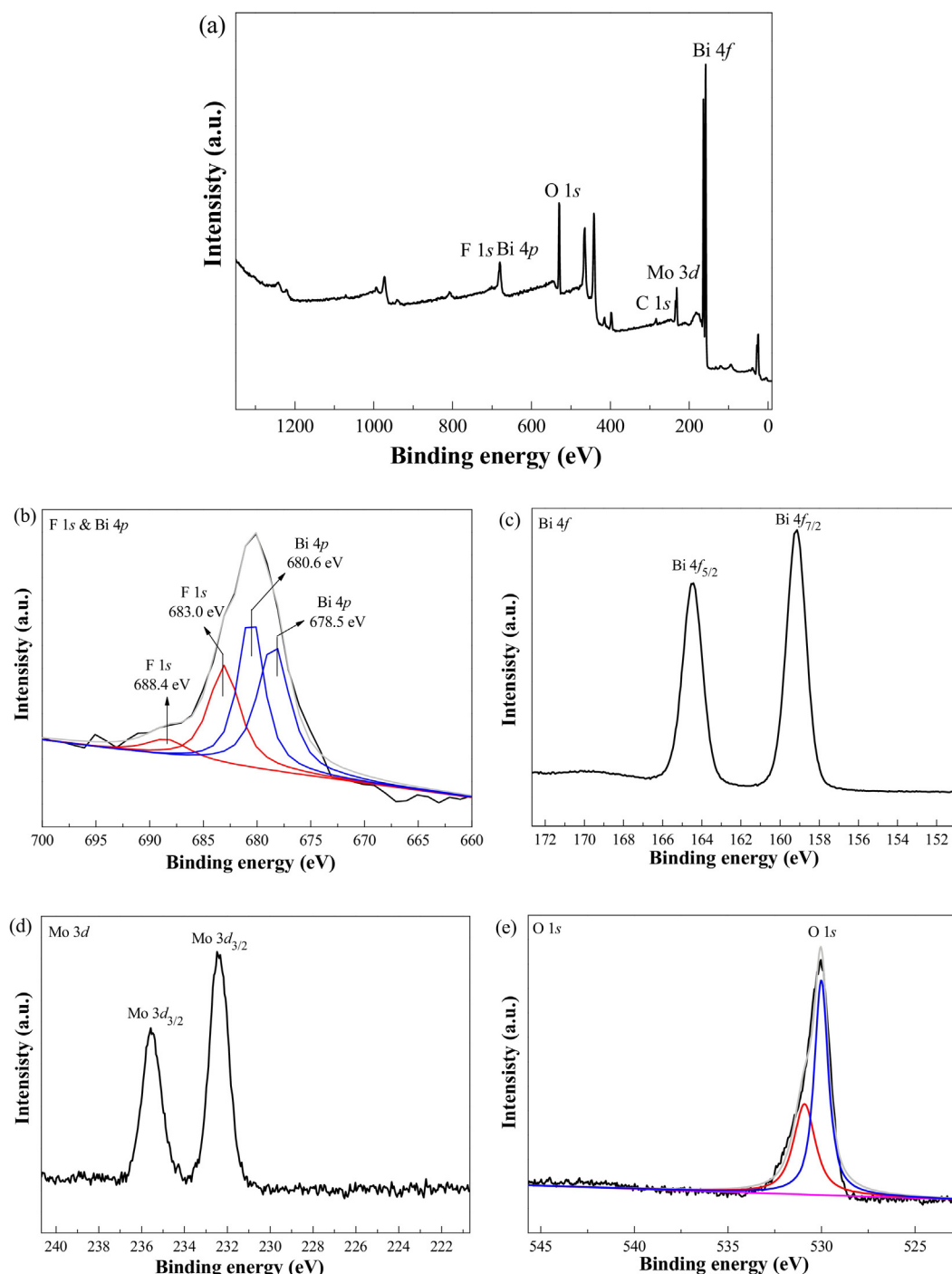
Fig. 6. XPS spectra of $F_{0.20}$-Bi_2MoO_6 sample. (a) Survey spectrum; (b) F 1s & Bi 4p; (c) Bi 4f; (d) O 1s; (e) Mo 3d.

respectively. Likewise, the degradation rate constant of bisphenol A over $F_{0.20}$-Bi_2MoO_6 increased 3.0, 2.7, and 5.4 times with respect to pure Bi_2MoO_6 under visible light, ultraviolet light, and simulated sunlight irradiation, respectively. Moreover, the 4-chlorophenol degradation rate constant of $F_{0.20}$-Bi_2MoO_6 reached $0.0132 \, min^{-1}$, which is 1.9 times higher than that of Bi_2MoO_6 $(0.0007 \, min^{-1})$ under simulated sunlight irradiation conditions.

3.8. Discussion on the enhanced degradation performance

To elucidate the mechanism for the enhanced photocatalytic performance, trapping experiments of reactive oxygen species in this F-Bi_2MoO_6 photocatalytic process were first carried out. Three quenchers, p-benzoquinone (BZQ, as $^{\bullet}O_2^{-}$ radicals scavenger, 1 mM), the *tert-butyl* alcohol (TBA, as the scavenger of $^{\bullet}OH$ radicals, 1 mM) and triethanolamine (TEOA, as the scavenger of h^+, 1 mM) were applied [54,55]. Fig. S3 shows that with the addition of TBA and BZQ, the degradation of RhB only decreased slightly. In contrast, the presence of trace TEOA caused a huge decrease in the degradation of RhB. Thus, we infer that photogenerated holes are the main active species for pollutant degradation in this F-Bi_2MoO_6 system, although $^{\bullet}OH$ and $^{\bullet}O_2^{-}$ radicals could also participate in the process of photocatalytic degradation reactions.
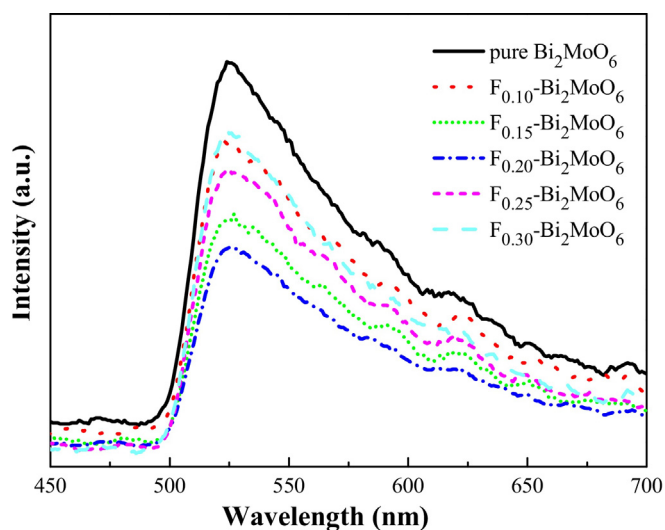
Fig. 7. The photoluminescence (PL) spectra of the pure Bi_2MoO_6 and F_R-Bi_2MoO_6 samples.

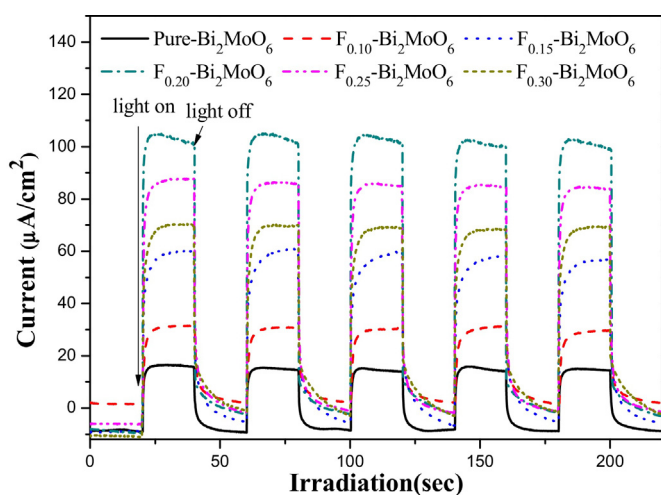**Fig. 8.** Photocurrent measurements of the pure Bi_2MoO_6 and F_R-Bi_2MoO_6 samples.

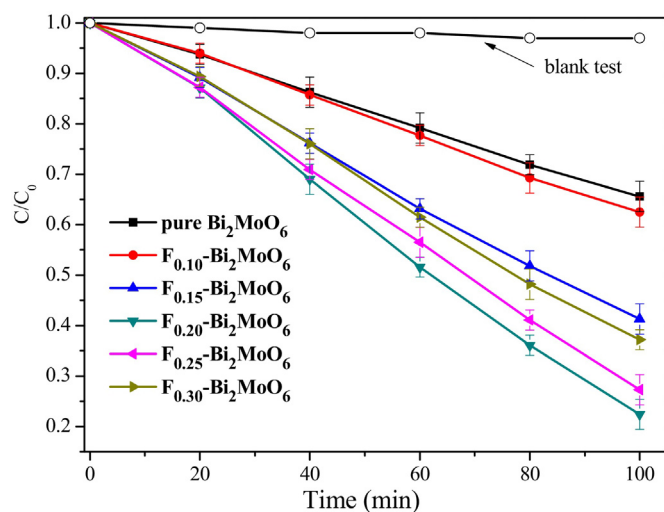**Fig. 9.** The photocatalytic performance test for pure Bi_2MoO_6 and F_R-Bi_2MoO_6 samples.

To further explore the radicals involved in the reactions and the effects of F doping on the radicals generation, electron spin resonance (ESR) was employed to probe the active oxygen species produced on the surface of the catalysts under simulated sunlight irradiation. In ESR studies, 5,5-dimethyl-1-pyrroline-N-oxide (DMPO) was used as the trapping agent. Fig. 11 presents the ESR signals of DMPO-•OH and DMPO-•O^{2-} of pure Bi_2MoO_6 and $F_{0.20}$-Bi_2MoO_6 samples before and after light illumination. In the dark, there were no ESR signals over all samples. Moreover, there were still no ESR signals of DMPO-•OH over pure Bi_2MoO_6 upon light irradiation (Fig. 11(a)), indicating that •OH is not the major oxidation species in this process similar to the Bi_2WO_6 system [56,57]. However, four strong characteristic signals of the DMPO-•OH adduct were observed over $F_{0.20}$-Bi_2MoO_6 catalysts. In Fig. 11(b), upon light illumination, ESR signals of DMPO-•O^{2-} over both Bi_2MoO_6 and $F_{0.20}$-Bi_2MoO_6 appear. Moreover, $F_{0.20}$-Bi_2MoO_6 displayed much stronger ESR signals than Bi_2MoO_6. Consequently, the results clearly show that •O^{2-} is another active species present in $F_{0.20}$-Bi_2MoO_6 photocatalysis. As former discussion, in this fluorinated Bi_2MoO_6, more oxygen vacancies could be produced because F^- ions have a much stronger affinity for electrons compared with O^{2-} ions. Oxygen vacancies can act as electron acceptors to trap the photogenerated electrons temporarily to reduce the surface recombination of electrons and holes. The trapped photogenerated electrons can reacted with the adsorbed O_2 to generate superoxide radicals (•O_2^-). On the other side, the fluoride anions adsorbed on the catalyst surface can play an important role in the separation of the photoexcited electron–hole pairs. Due to the high electronegativity of F^-, the surface-adsorbed F^- can trap electrons tightly, which largely benefited the separation of photogenerated electrons and holes. Therefore, more photogenerated electrons are available for •O_2^- generation. One possible route of •OH production over $F_{0.20}$-Bi_2MoO_6 would be that the electrons over the surface $F_{0.20}$-Bi_2MoO_6 could be trapped by adsorbed O_2 and H_2O to form •OH [58,59].

In order to realize the change of band positions of Bi_2MoO_6 induced by F doping, the band positions of pure Bi_2MoO_6 and $F_{0.20}$-Bi_2MoO_6 were calculated by the following formula:

$$E_{VB} = X - E_e + 0.5E_g \tag{2}$$

$$E_{CB} = E_{VB} - E_g \tag{3}$$

where E_{VB} and E_{CB} are the valence band (VB) edge potential and the conduction band (CB) edge potential, respectively, X is the absolute electronegativity of the semiconductor, E_e is the energy of free electrons on the hydrogen scale (the value of E_e is 4.5 eV), and E_g is the band gap energy of the semiconductor [60]. Herein, the X value for Bi_2MoO_6 is ~6.30 eV, the calculated result indicates that the CB and VB edge potentials of Bi_2MoO_6 are ~0.44 eV and ~3.16 eV, respectively. In addition, the Mott–Schottky curve obtained in an electrochemistry test was used to further reveal the changes of electronic structure of Bi_2MoO_6 after fluorination (as show in Fig. 12).

It was found that the Bi_2MoO_6 can be attributed to n-type semiconductor due to the positive slope of the linear plot. The flat band potentials of pure Bi_2MoO_6 and $F_{0.20}$-Bi_2MoO_6 film electrodes are 0.08 V and 0.23 V (vs Ag/AgCl, pH = 7), respectively. Generally, the conduction bands of n-type semiconductors are more negative about 0.1 V than the flat potentials [32,61]. Thus, the bottom of CB potentials of pure Bi_2MoO_6 and $F_{0.20}$-Bi_2MoO_6 are about -0.02 V and 0.13 V, respectively, which is equivalent to 0.18 V and 0.33 V versus the normal hydrogen electrode (NHE, pH = 7). Based on the UV–Vis DRS (Fig. 5), the calculated potentials of the top of VB for pure Bi_2MoO_6 and $F_{0.20}$-Bi_2MoO_6 are ~2.89 V and ~3.09 V (vs NHE, pH = 7), which is almost consistent with previous electronegativity calculation results. These results imply that the F doping could effectively improve the oxidation ability of holes in the valence
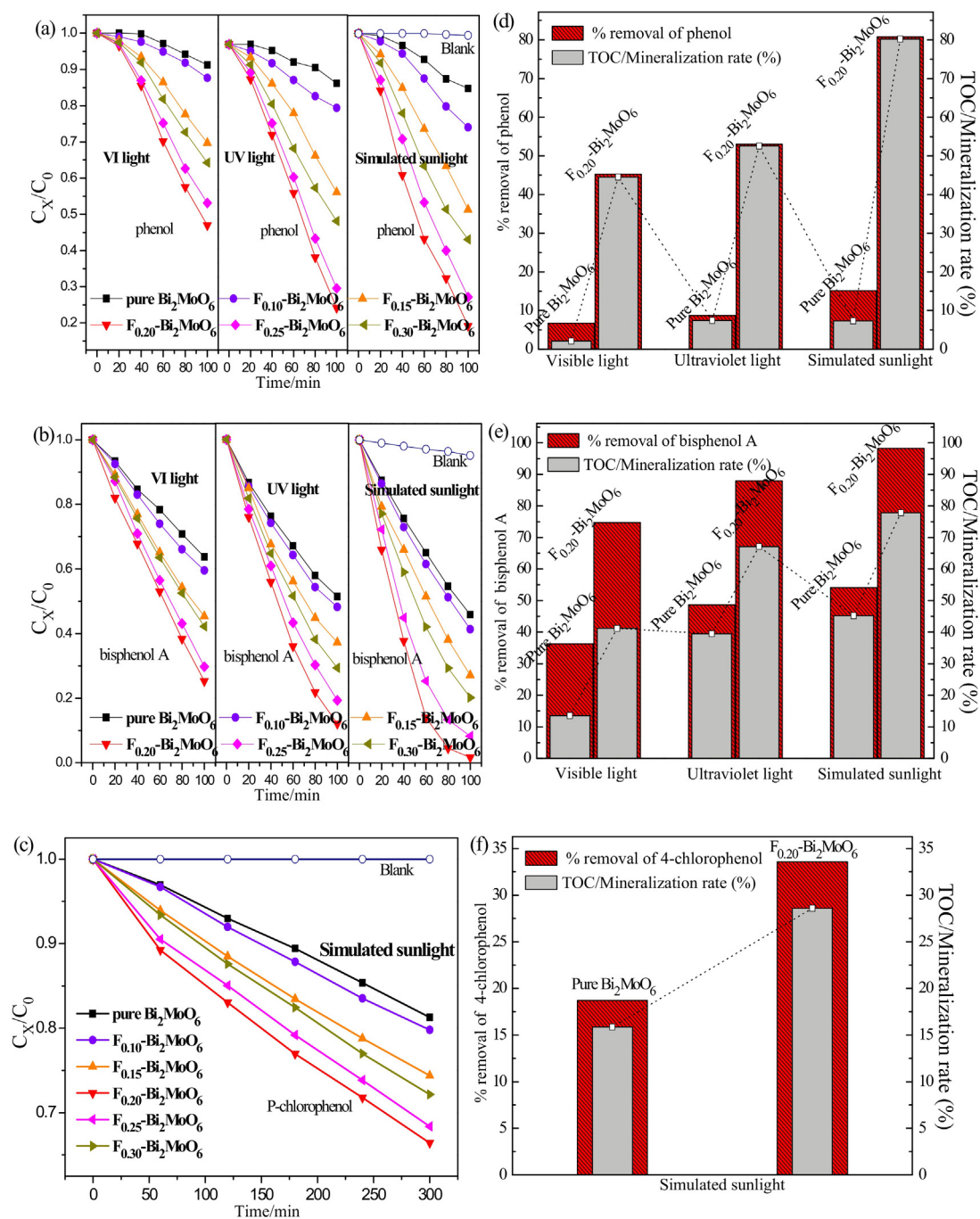
Fig. 10. The photocatalytic performances of pure Bi_2MoO_6 and F_R-Bi_2MoO_6 in the degradation of phenol, bisphenol A, and 4-chlorophenol under different light source irradiation. Concentration changes: (a) Phenol, (b) bisphenol A, (c) 4-chlorophenol; The degradation (%removal) and mineralization (%) over pure Bi_2MoO_6 and $F_{0.20}$-Bi_2MoO_6: (d) phenol, (e) bisphenol A, (f) 4-chlorophenol.

band of Bi_2MoO_6, which reached a similar result with the previously reported on $Bi_2WO_{6-X}F_{2X}$ [62].

On the basis of the results of the above catalyst characterization, catalyst activity, and active species trapping experiments, a possible photocatalytic reaction mechanism of F-Bi_2MoO_6 was proposed in Fig. 13.

Firstly, the results of XRD indicated that the average crystallite size of Bi_2MoO_6 was significantly decreased and crystallinity was increased by F^- doping. The decrease in crystal size and increase in crystallinity are beneficial for the transfer of photogenerated

carriers to the surface. Moreover, the replacement of O^{2-} anion by F^- could bring about anion oxygen vacancies in Bi_2MoO_6. Oxygen vacancies and fluoride anions adsorbed on the catalyst surface can trap electrons, hence largely boosting the separation of photogenerated electrons and holes. Thus, more active oxidizing species (h^+, •OH, •O_2^{2-}) were produced over $F_{0.20}$-Bi_2MoO_6 photocatalyst. Moreover, F-doping led to the change of band gap energy and more positive potential of VB over F-Bi_2MoO_6 was obtained, which improved the oxidation ability of holes in the degradation of the target organic pollutants.

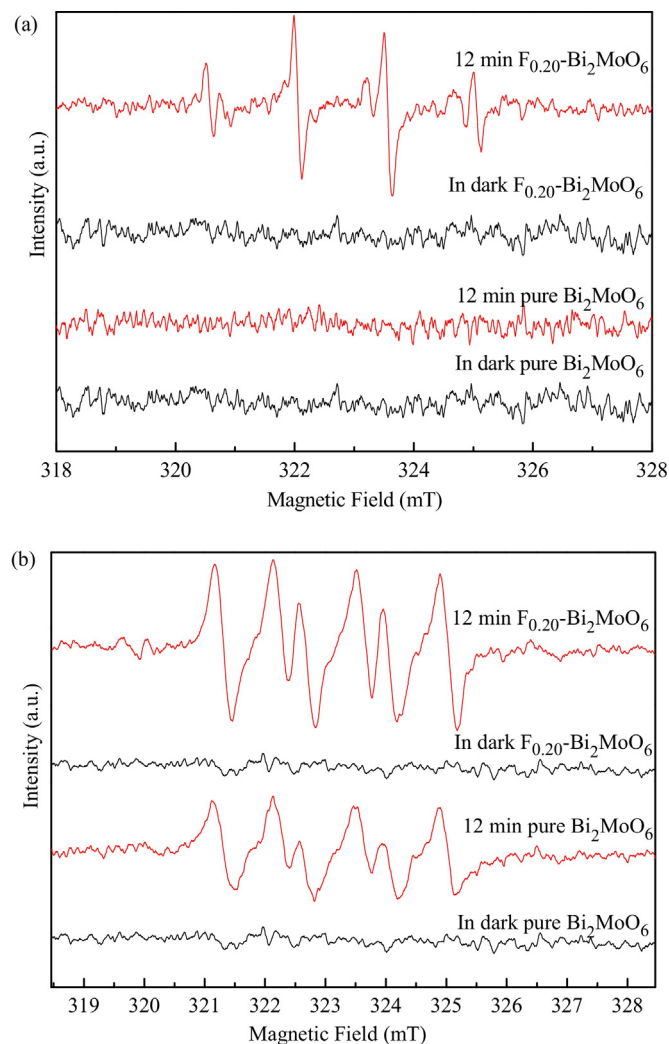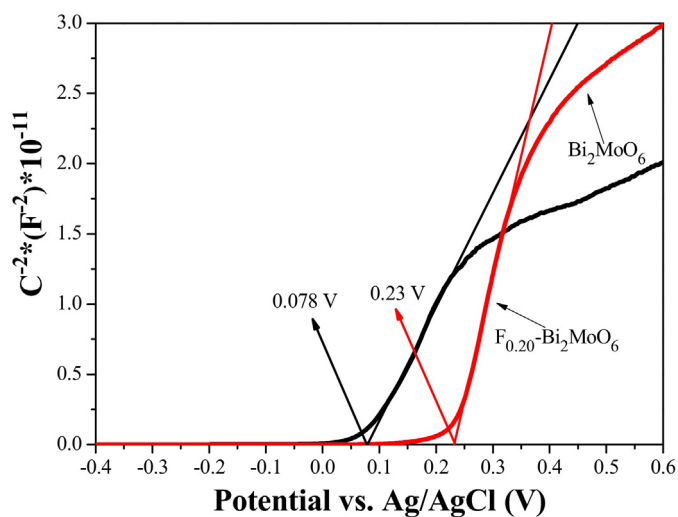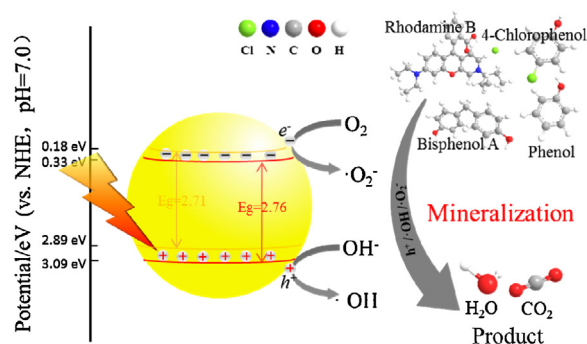Fig. 13. The suggested photocatalytic degradation mechanism of organic pollutants over F-Bi_2MoO_6 system.

4. Conclusions

In summary, a series of fluorinated Bi_2MoO_6 photocatalysts were prepared by a solvothermal-calcination process. Fluorination induced distinct variations in physicochemical properties of Bi_2MoO_6 crystal, e.g. lattice shrinkage, increase in crystallinity and decrease in surface area, blue-shift in light absorption threshold, and etc. The obtained F-Bi_2MoO_6 displayed significantly increased photocatalytic performance in removal of different water organic pollutants, e.g. dye, phenol, bisphenol A, and 4-chlorophenol. The enhancement of photocatalytic activity by F-doping could be attributed to the improved physicochemical properties and the high separation efficiency of photogenerated electron-hole pairs. The oxygen vacancies in Bi_2MoO_6 and fluoride anions adsorbed on the catalyst surface can trap electrons, largely boosting the separation of photogenerated electrons and holes and more active radicals (h^+, $^\bullet OH$, $^\bullet O_2^{2-}$) are available for organic pollutants degradation. In addition, F-doping lead to more positive potential of VB over F-Bi_2MoO_6, which improved the oxidation ability of holes in the valence band. This work provides a facile way to achieve highly efficient visible-light-driven photocatalysts with promising applications in water pollution purification.

Appendix A. Supplementary data

Supplementary data associated with this article can be found, in the online version, at http://dx.doi.org/10.1016/j.apcatb.2017.02.057.

References

[1] C.Y. Wang, L.Y. Zhu, M.C. Wei, P. Chen, G.Q. Shan, Water Res. 46 (2012) 845–853.
[2] P.M. Makinen, T.J. Theno, J.F. Ferguson, J.E. Ongerth, J.A. Puhakka, Environ. Sci. Technol. 27 (1993) 1434–1439.
[3] C.L. Yu, W.Q. Zhou, L.H. Zhu, G. Li, K. Yang, R.C. Jin, Appl. Catal. B 184 (2016) 1–11.
[4] S. Weon, W. Choi, Environ. Sci. Technol. 50 (2016) 2556–2563.

Fig. 11. ESR signals of (a) DMPO-$^\bullet OH$ and (b) DMPO-$^\bullet O^{2-}$ of pure Bi_2MoO_6 and $F_{0.20}$-Bi_2MoO_6 samples.

Fig. 12. Mott–Schottky (MS) plots for the pure Bi_2MoO_6 and $F_{0.20}$-Bi_2MoO_6 film electrodes.

[5] H. Barndõk, D. Hermosilla, C. Han, D.D. Dionysiou, C. Negro, Á. Blanco, Appl. Catal. B 180 (2016) 44–52.
[6] C.Y. Wang, H. Zhang, F. Li, L.Y. Zhu, Environ. Sci. Technol. 44 (2010) 6843–6848.
[7] K. Yu, S.G. Yang, C. Liu, H.Z. Chen, H. Li, C. Sun, S.A. Boyd, Environ. Sci. Technol. 46 (2012) 7318–7326.
[8] X.Z. Li, H. Liu, L.F. Cheng, H.J. Tong, Environ. Sci. Technol. 37 (2003) 3989–3994.
[9] C.L. Yu, W.Q. Zhou, H. Liu, Y. Liu, D.D. Dionysiou, Chem. Eng. J. 287 (2016) 17–129.
[10] C. Zhao, M. Pelaez, D.D. Dionysiou, S.C. Pillai, J.A. Byrne, K.E. O'Shea, Catal. Today 224 (2014) 70–76.
[11] J. Ma, L.Z. Zhang, Y.H. Wang, S.L. Lei, X.B. Luo, S.H. Chen, G.S. Zeng, J.P. Zou, S.L. Luo, C.T. Au, Chem. Eng. J. 251 (2014) 371–380.
[12] C.L. Yu, Q.Z. Fan, Y. Xie, J.C. Chen, Q. Shu, J.C. Yu, J. Hazard. Mater. 237–238 (2012) 38–45.
[13] L.F. Chiang, R.A. Doong, J. Hazard. Mater. 277 (2014) 84–92.
[14] M.V. Carević, N.D. Abazović, T.B. Novaković, V.B. Pavlović, M.I. Čomor, Appl. Catal. B 195 (2016) 112–120.
[15] V. Vaiano, O. Sacco, D. Sannino, P. Ciambelli, Chem. Eng. J. 261 (2015) 3–8.
[16] S. Zheng, W.J. Jiang, Y. Cai, D.D. Dionysiou, K.E. O'Shea, Catal. Today 224 (2014) 83–88.
[17] A. Kaur, S.K. Kansal, Chem. Eng. J. 302 (2016) 194–203.
[18] M. Antonopoulou, P. Karagianni, I.K. Konstantinou, Appl. Catal. B 192 (2016) 152–160.
[19] T. Fotiou, T.M. Triantis, T. Kaloudis, K.E. O'Shea, D.D. Dionysiou, A. Hiskia, Water Res. 90 (2016) 52–61.
[20] R. Fagan, D.E. Mccormack, D.D. Dionysiou, S.C. Pillai, Mater. Sci. Semicond. Process 42 (2016) 2–14.
[21] X.X. He, A.A. delaCruz, A. Hiskia, T. Kaloudis, K. O'Shea, D.D. Dionysiou, Water Res. 74 (2015) 227–238.
[22] S. In, A. Orlov, R. Berg, F. García, S. Pedrosa-Jimenez, M.S. Tikhov, D.S. Wright, R.M. Lambert, J. Am. Chem. Soc. 129 (2007) 13790–13791.
[23] C.L. Yu, L.F. Wei, J.C. Chen, Y. Xie, W.Q. Zhou, Q.Z. Fan, Ind. Eng. Chem. Res. 53 (2014) 5759–5766.
[24] X.C. Wang, K. Maeda, A. Thomas, K. Takanabe, G. Xin, J.M. Carlsson, K. Domen, M. Antonietti, Nature Mater. 8 (2009) 76–80.
[25] C.L. Yu, G. Li, S. Kumar, K. Yang, R.C. Jin, Adv. Mater. 26 (2014) 892–898.
[26] C.L. Yu, G. Li, S. Kumar, H. Kawasaki, R.C. Jin, J. Phys. Chem. Lett. 4 (2013) 2847–2852.
[27] K.F. Wu, G.J. Liang, Q.Y. Shang, Y.P. Ren, D.G. Kong, T.Q. Lian, JACS 137 (2015) 12792–12795.
[28] S. Seth, N. Mondal, S. Patra, A. Samanta, J. Phys. Chem. Lett. 7 (2016) 266–271.
[29] S.Q. Jiang, L. Wang, W.C. Hao, W.X. Li, H.J. Xin, W.W. Wang, T.M. Wang, J. Phys. Chem. J 119 (2015) 14094–14101.
[30] J.X. Xia, J. Di, H.T. Li, H. Xu, H.M. Li, S.J. Guo, Appl. Catal. B 181 (2016) 260–269.
[31] M.L. Niu, R.S. Zhu, F. Tian, K.L. Song, G. Cao, F. Ouyang, Catal. Today 258 (2015) 585–594.
[32] Y.F. Liu, Y.H. Lv, Y.Y. Zhu, D. Liu, R.L. Zong, Y.F. Zhu, Appl. Catal. B 147 (2014) 851–857.
[33] M. Qamar, R.B. Elsayed, K.R. Alhooshani, M.I. Ahmed, D.W. Bahnemann, ACS Appl. Mater. Interfaces 7 (2015) 1257–1269.
[34] D.J. Wang, H.D. Shen, L. Guo, C. Wang, F. Fu, Y.C. Liang, RSC Adv. 6 (2016) 71052–71060.
[35] J.L. Zhang, L.S. Zhang, N. Yu, K.B. Xu, S.J. Lia, H.L. Wang, J.S. Liu, RSC Adv. 5 (2015) 75081–75088.
[36] H.P. Li, J.Y. Liu, W.G. Hou, N. Du, R.J. Zhang, X.T. Tao, Appl. Catal. B 160 (2014) 89–97.
[37] Y. Chen, G. Tian, Y. Shi, Y. Xiao, H. Fu, Appl. Catal. B 164 (2015) 40–47.
[38] Y.S. Xu, Z.J. Zhang, W.D. Zhang, Mater. Res. Bull 48 (2013) 1420–1427.
[39] Y. Feng, X. Yan, C.B. Liu, Y.Z. Hong, L. Zhu, M.J. Zhou, W.D. Shi, Appl. Surf. Sci. 353 (2015) 87–94.
[40] X. Ding, W. Ho, J. Shang, L. Zhang, Appl. Catal. B 182 (2016) 316–325.
[41] C.L. Yu, Z. Wu, R.Y. Liu, H.B. He, W.H. Fan, S.S. Xue, J. Phys. Chem. Solids 93 (2016) 7–13.
[42] Z. Dai, F. Qin, H.P. Zhao, J. Ding, Y.L. Liu, R. Chen, ACS Catal. 65 (2016) 3180–3192.
[43] X.B. Zhang, L. Zhang, J.S. Hu, X.H. Huang, RSC Adv. 6 (2016) 32349–32357.
[44] X. Zhao, J.H. Qu, H.J. Liu, Z.M. Qiang, R.P. Liu, C.Z. Hu, Appl. Catal. B 91 (2009) 539–545.
[45] H.Y. Jiang, J.J. Liu, K. Cheng, W.B. Sun, J. Lin, J. Phys. Chem. C 117 (2013) 20029–20036.
[46] J. Podporska-Carroll, A. Myles, B. Quilty, D.E. McCormack, R. Fagan, S.J. Hinder, D.D. Dionysiou, S.C. Pillai, J. Hazard. Mater. 59 (2015) 669–678.
[47] G. Huang, Y. Zhu, J. Phys. Chem. C 111 (2007) 11952–11958.
[48] H.B. Fu, S.C. Zhang, T.G. Xu, Y.F. Zhu, J.M. Chen, Environ. Sci. Technol. 42 (2008) 2085–2091.
[49] J.L. Long, S.C. Wang, H.J. Chang, B.Z. Zhao, B.T. Liu, Y.G. Zhou, W. Wei, X.X. Wang, L. Huang, W. Huang, Small 10 (2014) 2791–2795.
[50] L. Zhang, T. Xu, X. Zhao, Y. Zhu, Appl. Catal. B 98 (2010) 138–146.
[51] J.C. Yu, J. Yu, W. Ho, Z. Jiang, L. Zhang, Chem. Mater. 14 (2002) 3808–3816.
[52] G.H. Tian, Y.J. Chen, R.T. Zhai, J. Zhou, W. Zhou, R.H. Wang, K. Pan, C.G. Tian, H.G. Fu, J. Mater. Chem. A 1 (2013) 6961–6968.
[53] H.W. Huang, K. Liu, K. Chen, Y.L. Zhang, Y.H. Zhang, S.C. Wang, J. Phys. Chem. C 118 (2014) 14379–14387.
[54] N. Tian, Y.H. Zhang, H.W. Huang, Y. He, Y.X. Guo, J. Phys. Chem. C 118 (2014) 15640–15648.
[55] Q.B. Li, X. Zhao, J. Yang, C.J. Jia, Z. Jin, W.L. Fan, Nanoscale 7 (2015) 18971–18983.
[56] Z.J. Zhang, W.Z. Wang, E. Gao, M. Shang, J.H. Xu, Materials 196 (2011) 255–262.
[57] H.B. Fu, C.S. Pan, W.Q. Yao, Y.F. Zhu, J. Phys. Chem. B 109 (2005) 22432–22439.
[58] X.X. Li, S.M. Fang, L. Ge, C.C. Han, P. Qiu, W.L. Liu, Appl. Catal. B 176/177 (2015) 62–69.
[59] X.J. Bai, L. Wang, R.L. Zong, Y.F. Zhu, J. Phys. Chem. C 117 (2013) 9952–9961.
[60] H.W. Huang, L.Y. Liu, Y.H. Zhang, N. Tian, J. Alloys Compd. 619 (2015) 807–811.
[61] X.L. Jin, L.Q. Ye, H. Wang, Y.R. Su, H.Q. Xie, Z.G. Zhong, H. Zhang, Appl. Catal. B 165 (2015) 668–675.
[62] R. Shi, G.L. Huang, J. Lin, Y.F. Zhu, J. Phys. Chem. C 113 (2009) 19633–19638.

Update

Applied Catalysis B: Environmental

Corrigendum

Corrigendum to "Novel fluorinated Bi_2MoO_6 nanocrystals for efficient photocatalytic removal of water organic pollutants under different light source illumination" [Appl. Catal. B: Environ. 209 (2017) 1–11]

Changlin Yu[a],[*], Zhen Wu[a], Renyue Liu[a], Dionysios D. Dionysiou[b], Kai Yang[a], Chunying Wang[c], Hong Liu[d],[*]

[a] School of Metallurgy and Chemical Engineering, Jiangxi University of Science and Technology, Ganzhou 341000, China
[b] Environmental Engineering and Science Program, Department of Biomedical, Chemical and Environmental Engineering, University of Cincinnati, Cincinnati, OH 45221, United States
[c] School of Resources and Environmental Engineering, Jiangxi University of Science and Technology, Ganzhou 341000, China
[d] School of Chemical Engineering and Technology, Sun Yat-Sen University, Zhuhai, 519082, China

The authors regret < A mistake in Fig. 11 (Applied Catalysis B: Environmental 209 (2017) 1–11) was made in the article, the same ESR signals in the dark for (a) DMPO-$^\cdot$OH and (b) DMPO-$^\cdot$O^{2-} over Bi_2MoO_6 and $F_{0.20}$-Bi_2MoO_6 samples. Although there is no ESR signals in the dark for Bi_2MoO_6 and $F_{0.20}$-Bi_2MoO_6 samples, Tianhe Research Assistance Centre (Shandong Province, China) provided the same background data for the ESR test for $^\cdot$O^{2-} in the dark for Bi_2MoO_6 and $F_{0.2}$-Bi_2MoO_6 samples and the same data for the ESR test for $^\cdot$OH$^-$ in the dark for Bi_2MoO_6 and $F_{0.2}$-Bi_2MoO_6 samples. We apologized for this oversight and any inconvenience caused. We have prepared new samples and sent the samples to the Tianhe Research Assistance Centre to check again for new samples. >
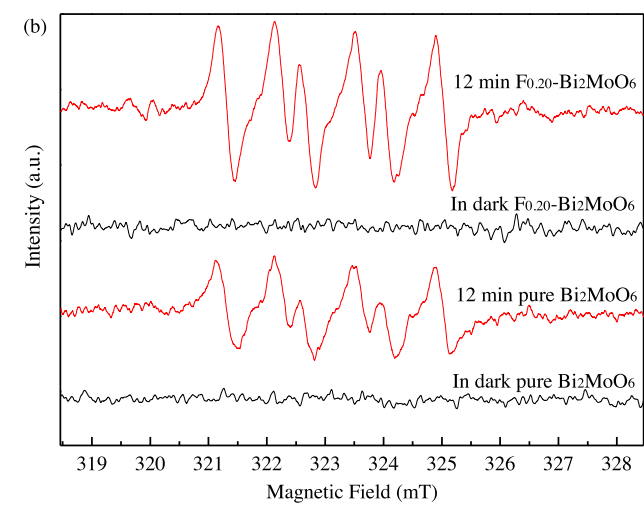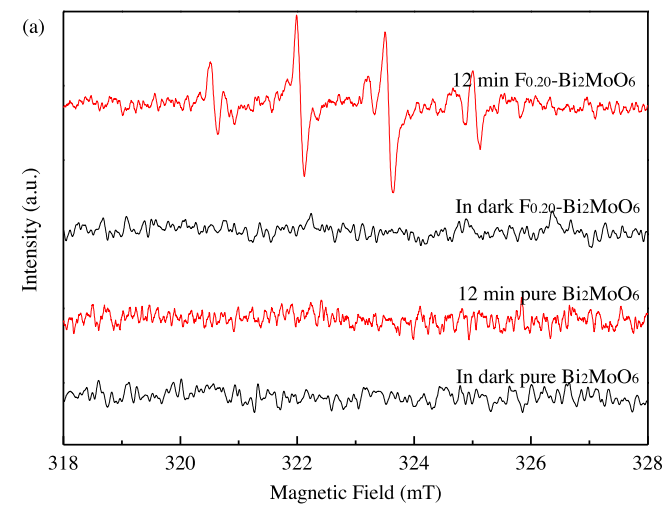
(a)

(b)

Corrected Fig. 11 ESR signals of (a) DMPO-$\cdot$OH and (b) DMPO-$\cdot O^{2-}$ of pure Bi_2MoO_6 and $F_{0.20}$-Bi_2MoO_6 samples.